SURFACE PHYSICS

A.V. KOROTUN,[1, 2] YA.V. KARANDAS,[1] V.I. REVA [1]

[1] National University "Zaporizhzhia Polytechnic"
 (64, Zhukovs'kogo Str., Zaporizhzhya 69063, Ukraine)
[2] G.V. Kurdyumov Institute for Metal Physics, Nat. Acad. of Sci. of Ukraine
 (36, Akademika Vernads'kogo Blvd., Kyiv 03142, Ukraine; e-mail: andko@zp.edu.ua)

ANALYTICAL THEORY OF PLASMON EFFECTS IN ROD-LIKE METAL NANOPARTICLES. THE EQUIVALENT-SPHEROID MODEL

In the framework of the model of equivalent prolate spheroid, analytical expressions for the polarizabilities of rod-like metal structures have been derived, which substantially simplified the calculation of their optical characteristics. The frequency dependences of the transverse and longitudinal components of the polarizability tensor, as well as the absorption and scattering cross-sections, are calculated for prolate spheroids, cylinders, and spherocylinders. The changes in the positions of the maxima of the imaginary part of the polarizability tensor components and the changes of the absorption and scattering cross-sections with variations in the size, shape, and material of nanoparticles are analyzed. It is found that the position of the transverse surface plasmon resonance (SPR) in rod-like nanoparticles of the considered shapes is practically insensitive to the changes of their semiaxes, whereas the increase of the aspect ratio leads to a "blue" shift of the longitudinal SPR. It is shown that the use of the model of effective prolate spheroid provides satisfactory agreement with experimental data obtained at the longitudinal SPR frequencies and does not require the application of complicated computational methods.

K e y w o r d s: polarizability tensor, absorption and scattering cross-sections, equivalent prolate spheroid, relaxation rate, plasmon resonance.

1. Introduction

The interaction between light and matter at the sub-wavelength level opens new possibilities for optical probing, accumulation of light energy, and development of new optical devices [1–3]. Resonance nanostructures and nanoparticles can enhance the optical response and improve the parameters of photonic devices [4–8].

Localized surface plasmon resonances (SPRs) can be excited at the surface of metal nanoparticles whose sizes extend from a few to hundred nanometers. As a result, a significant enhancement of electromagnetic fields takes place near the nanoparticle surface [9, 10].

Nowadays, the methods of wet chemical synthesis allow plasmonic nanoparticles with a wide variety of their shapes – including spheres [11], triangles [12], prisms [13], rods [14], and cubes [15] – and with controlled dimensions and narrow size distributions to be manufactured. The production of such a variety of nanostructures favors their wide application in optoelectronics and nanophotonics [16]. This occurs, because the SPR frequency is determined by the dielectric function of the metal and the dielectric permittivity of the environment; besides it also strongly depends on the nanostructure size and shape [17–22]. For instance, in the case of spherical nanoparticles, the SPR emerges if the real part of the dielectric permittivity of the nanoparticle, being taken with the
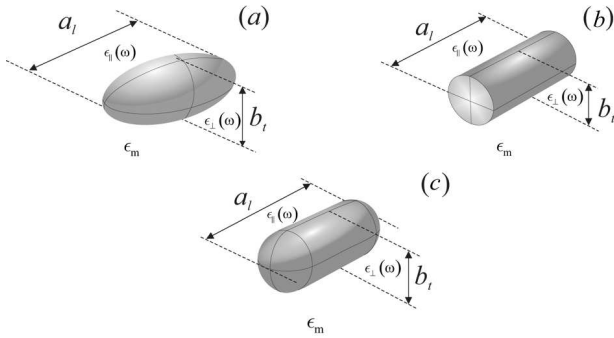
Fig. 1. Geometry of rod-like nanoparticles: prolate spheroid (*a*), finite-length cylinder (*b*), and spherocylinder (*c*)

minus sign, is equal to twice the value of the dielectric permittivity of the environment (the Frölich condition). On the other hand, in the case of non-spherical nanoparticles, the electron oscillations are anisotropic and localized either along the principal axes [23, 24] or at the nanoparticle boundaries and corners [25], which leads to an additional SPR dependence on depolarization factors, as well as the SPR split into the longitudinal and transverse modes. Such features can give rise, for example, to the enhancement of the Raman scattering effect and, in particular, to the giant Raman scattering (GRS) [26, 27].

In the majority of works aimed at studying the optical response of rod-shaped nanoparticles, the model of prolate spheroid [28, 29] is used, because the corresponding electrostatic problem has analytical solutions. According to this model, the aspect ratio of a rod-shaped particle is equal to the ratio between the semi-axes of this spheroid. However, currently the opinion prevails [30–32] that this model does not accurately describe some features in the experimentally obtained optical properties of nanorods. For instance,

Table 1. Geometric parameters of rod-like nanoparticles (*a* and *b* are the major and minor, respectively, semi-axes of the spheroid; *r* and *l* are the radius and the length of the cylinder (spherocylinder))

Shape	Sizes		Volume
	a_l	b_t	V
Prolate spheroid	$2a$	$2b$	$\frac{4\pi}{3}\pi a^2 b$
Cylinder	l	$2r$	$\pi r^2 l$
Spherocylinder	$l + 2r$	$2r$	$\pi r^2 \left(l + \frac{4}{3} r\right)$

in work [30], by comparing the positions of the longitudinal SPR for cylinders, spherocylinders, and prolate spheroids with the same aspect ratio, the cited authors came to the conclusion that this position depends on the object geometry. In addition, it was found that the model of equivalent prolate spheroid provides a better approximation to experimental results than the model of prolate spheroid does.

In this connection, a conclusion was drawn in work [33] that the equalities of the corresponding axial moments of inertia of the equivalent prolate spheroids and rod-like nanoparticles comprise a natural criterion for the comparison of metallic rod-like structures. This criterion can be used to obtain expressions for the effective aspect ratios of prolate spheroids equivalent to finite-length cylinders and spherocylinders.

Therefore, the aim of this work is to study the optical properties of rod-like metal particles using the model of equivalent prolate spheroid.

2. Formulation of the Problem and Main Relationships

Consider a metallic rod-like finite-length particle embedded into a medium with the dielectric constant ϵ_{m} (Fig. 1). In order to analyze the particle geometry effect on the optical properties of such particles, finite-length cylinders and spherocylinders, as well as an equivalent to them prolate spheroid, will be considered. The geometric parameters of the indicated objects are quoted in Table 1.

The starting point for our research includes the following formulas for the absorption and scattering cross-sections of the prolate spheroid embedded in a dielectric medium [10]:

$$C_{\mathrm{abs}} = \frac{\omega\sqrt{\epsilon_{\mathrm{m}}}}{c}\,\mathrm{Im}\left(\frac{2}{3}\alpha_\perp + \frac{1}{3}\alpha_\parallel\right), \tag{1}$$

$$C_{\mathrm{sca}} = \frac{\omega^4\epsilon_{\mathrm{m}}^2}{6\pi c^4}\left(\frac{2}{3}|\alpha_\perp|^2 + \frac{1}{3}|\alpha_\parallel|^2\right), \tag{2}$$

where c is the speed of light,

$$\alpha_{\perp(\parallel)} = V\frac{\epsilon_{\perp(\parallel)}(\omega) - \epsilon_{\mathrm{m}}}{\epsilon_{\mathrm{m}} + \mathcal{L}_{\perp(\parallel)}\left(\epsilon_{\perp(\parallel)}(\omega) - \epsilon_{\mathrm{m}}\right)} \tag{3}$$

are the diagonal components of the spheroid polarizability tensor, V is the spheroid volume,

$$\mathcal{L}_\parallel = \frac{1 - e_p^2}{2e_p^3}\left(\ln\frac{1 + e_p}{1 - e_p} - 2e_p\right), \tag{4}$$

and

$$\mathcal{L}_\perp = \frac{1}{2}\left(1 - \mathcal{L}_\parallel\right), \tag{5}$$

are the depolarization factors of the prolate spheroid, and e_p is the spheroid eccentricity. The diagonal components of the permittivity tensor are described in the framework of the Drude theory by the relationships

$$\epsilon_{\perp(\parallel)}(\omega) = \epsilon^\infty - \frac{\omega_p^2}{\omega\left(\omega + i\gamma_{\text{eff}}^{\perp(\parallel)}\right)}. \tag{6}$$

where ϵ^∞ is the component describing the contribution of the ionic core to the dielectric permittivity, $\omega_p = \left(e^2 n_e/\epsilon_0 m^*\right)^{1/2}$ is the plasma frequency, n_e the concentration of conduction electrons, m^* the effective electron mass, ϵ_0 the electrical constant, and $\gamma_{\text{eff}}^{\perp(\parallel)}$ the effective transverse (longitudinal) relaxation rate. For nanoscale objects, the latter is determined as follows:

$$\gamma_{\text{eff}}^{\perp(\parallel)} = \gamma_{\text{bulk}} + \gamma_{\text{s}}^{\perp(\parallel)} + \gamma_{\text{rad}}^{\perp(\parallel)}, \tag{7}$$

where γ_{bulk} and $\gamma_{\text{s}}^{\perp(\parallel)}$ are the bulk and surface, respectively, relaxation rates; and $\gamma_{\text{rad}}^{\perp(\parallel)}$ is the radiation damping rate.

For a prolate spheroid, the surface relaxation and radiation damping rates are determined by the formulas [22]

$$\gamma_{\text{s}}^{\perp(\parallel)} = \frac{\mathcal{L}_{\perp(\parallel)}\sigma_{\perp(\parallel)}}{\epsilon_0\left[\epsilon_{\text{m}} + \mathcal{L}_{\perp(\parallel)}\left(1 - \epsilon_{\text{m}}\right)\right]}, \tag{8}$$

$$\gamma_{\text{rad}}^{\perp(\parallel)} = \frac{2V}{9\pi\epsilon_0}\left(\frac{\omega_p}{c}\right)^3 \frac{\mathcal{L}_{\perp(\parallel)}\sigma_{\perp(\parallel)}}{\sqrt{\epsilon_{\text{m}}\left[\epsilon^\infty + \left(\frac{1}{\mathcal{L}_{\perp(\parallel)}} - 1\right)\epsilon_{\text{m}}\right]}}. \tag{9}$$

These formulas include the diagonal components $\sigma_\parallel$ and $\sigma_\perp$ of the conductivity tensor of prolate spheroid, which can be determined using the relationships obtained in works [34, 35],

$$\sigma_\parallel = \frac{9n_e e^2}{2m^*\omega}\left(\frac{\omega}{\nu_{s,\perp}}\right)^2 \frac{1}{e_p^3}\int\limits_{\frac{\omega}{\nu_{s,\perp}}}^{\frac{\omega}{\nu_{s,\parallel}}} \frac{dx}{x^4}\left[1 - \left(\frac{\omega}{\nu_{s,\perp}x}\right)^2\right]^{\frac{1}{2}} \times$$

$$\times\left\{1 - \frac{2}{x}\sin x + \frac{2}{x^2}\left(1 - \cos x\right)\right\}, \tag{10}$$

$$\sigma_\perp = \frac{9n_e e^2}{4m^*\omega}\left(\frac{\omega}{\nu_{s,\perp}}\right)^2 \frac{e_p^2 - 1}{e_p^3}\int\limits_{\frac{\omega}{\nu_{s,\perp}}}^{\frac{\omega}{\nu_{s,\parallel}}} \frac{dx}{x^4}\frac{1 - \left(\frac{\omega}{\nu_{s,\parallel}x}\right)^2}{\left[1 - \left(\frac{\omega}{\nu_{s,\perp}x}\right)^2\right]^{\frac{1}{2}}} \times$$

$$\times\left\{1 - \frac{2}{x}\sin x + \frac{2}{x^2}\left(1 - \cos x\right)\right\}, \tag{11}$$

where $\nu_{s,\perp}$ and $\nu_{s,\parallel}$ are the frequencies of individual electron oscillations along the corresponding spheroid axes.

Now let us proceed to the calculation of the effective aspect ratio for a prolate spheroid equivalent to a finite-length cylinder and a spherocylinder. For this purpose, let us write down expressions for the axial moments of inertia of those objects [33]:

$$I_{\text{sph}}^x = \frac{m_{\text{sph}}}{5}(a^2 + b^2), \quad I_{\text{sph}}^z = \frac{2m_{\text{sph}}}{5}b^2, \tag{12}$$

$$I_{\text{cyl}}^x = \frac{m_{\text{cyl}}}{12}(3r^2 + l^2), \quad I_{\text{cyl}}^z = \frac{m_{\text{cyl}}}{2}r^2, \tag{13}$$

$$I_{\text{sphcyl}}^x = \pi\mu r^5 \times$$

$$\times\left\{\frac{\delta}{6}(3 + 4\delta^2) + \frac{4}{3}\left(\frac{83}{320} + \left(\delta + \frac{3}{8}\right)^2\right)\right\}, \tag{14}$$

$$I_{\text{sphcyl}}^z = \pi\mu r^5\left(\frac{\delta}{6} + \frac{8}{15}\right), \tag{15}$$

where $\delta \equiv 1 - \varrho$, and μ is the density of the spherocylinder material. Equating the ratios I^x/I^z between the axial moments of inertia and taking into account that the aspect ratio equals

$$\varrho = \frac{2r}{l} \tag{16a}$$

for the cylinder and

$$\varrho = \frac{2r}{l + 2r} \tag{16b}$$

for the spherocylinder, we obtain effective aspect ratios for spheroids equivalent to cylinders,

$$\varrho_{\text{eff}} = \frac{\sqrt{3}}{2}\varrho, \tag{17a}$$

and spherocylinders,

$$\varrho_{\text{eff}} = \left(1 + \frac{4\delta}{3}\frac{\delta^2 + \delta + \frac{3}{4}}{\delta + \frac{8}{15}}\right)^{-\frac{1}{2}}. \tag{17b}$$

Neglecting the oscillating terms owing to their smallness in comparison with the unity in the braces in Eqs. (10) and (11), and calculating the integrals, we obtain the following expressions for the diagonal

components of the conductivity tensor of the equivalent prolate spheroid:

$$\sigma_{\perp(\parallel)}(\omega) = \frac{9}{16}\epsilon_0\left(\frac{\omega_p}{\omega}\right)^2\nu_{s,\perp}F_{\perp(\parallel)}(\varrho_{\mathrm{eff}}),\qquad(18)$$

where

$$F_\perp(\varrho_{\mathrm{eff}}) = \left(1-\varrho_{\mathrm{eff}}^2\right)^{-\frac{3}{2}}\times$$

$$\times\left\{\varrho_{\mathrm{eff}}\left(\frac{3}{2}-\varrho_{\mathrm{eff}}^2\right)\sqrt{1-\varrho_{\mathrm{eff}}^2}+\right.$$

$$\left.+2\left(\frac{3}{4}-\varrho_{\mathrm{eff}}^2\right)\left(\frac{\pi}{2}-\arcsin\varrho_{\mathrm{eff}}\right)\right\};\qquad(19)$$

$$F_\parallel(\varrho_{\mathrm{eff}}) = \left(1-\varrho_{\mathrm{eff}}^2\right)^{-\frac{3}{2}}\times$$

$$\times\left\{\frac{\pi}{2}-\arcsin\varrho_{\mathrm{eff}}+\varrho_{\mathrm{eff}}\left(1-2\varrho_{\mathrm{eff}}^2\right)\sqrt{1-\varrho_{\mathrm{eff}}^2}\right\},\quad(20)$$

and for the frequency of individual oscillations in the transverse direction equals [34]:

$$\nu_{s,\perp} = \frac{v_{\mathrm{F}}}{2b_t},\qquad(21)$$

where v_{F} is the Fermi velocity of electrons, and expressions for b_t are quoted in Table 1.

By substituting relationships (18) into formulas (8) and (9), we obtain the following expressions: for the surface relaxation rate,

$$\gamma_{\mathrm{s}}^{\perp(\parallel)} = \frac{9}{16}\frac{\mathcal{L}_{\perp(\parallel)}}{\epsilon_0\left[\epsilon_{\mathrm{m}}+\mathcal{L}_{\perp(\parallel)}\left(1-\epsilon_{\mathrm{m}}\right)\right]}\times$$

$$\times\frac{v_{\mathrm{F}}}{2r}\left(\frac{\omega_p}{\omega}\right)^2F_{\perp(\parallel)}(\varrho_{\mathrm{eff}});\qquad(22)$$

and for the radiation damping rate,

$$\gamma_{\mathrm{rad}}^{\perp(\parallel)} = \frac{V}{8\pi}\frac{\mathcal{L}_{\perp(\parallel)}}{\sqrt{\epsilon_{\mathrm{m}}\left[\epsilon^\infty+\left(\frac{1}{\mathcal{L}_{\perp(\parallel)}}-1\right)\epsilon_{\mathrm{m}}\right]}}\times$$

$$\times\frac{v_{\mathrm{F}}}{2r}\left(\frac{\omega_p}{c}\right)^3\left(\frac{\omega_p}{\omega}\right)^2F_{\perp(\parallel)}(\varrho_{\mathrm{eff}}),\qquad(23)$$

Table 2. **Parameters of metals**

Parameter	Al	Cu	Au	Ag
r_s/a_0	2.07	2.11	3.01	3.02
m^*/m_e	1.06/1.48/1.60	1.49	0.99	0.96
ϵ^∞	0.7	12.03	9.84	3.7
$\gamma_{\mathrm{bulk}}, 10^{13}\ \mathrm{s}^{-1}$	12.50	3.70	3.45	2.50

where the dependence of the depolarization factor $\mathcal{L}_\parallel$ on the effective aspect ratio looks like

$$\mathcal{L}_\parallel = \frac{\varrho_{\mathrm{eff}}^2}{2\left(1-\varrho_{\mathrm{eff}}^2\right)^{\frac{3}{2}}}\left(\ln\frac{1+\sqrt{1-\varrho_{\mathrm{eff}}^2}}{1-\sqrt{1-\varrho_{\mathrm{eff}}^2}}-2\sqrt{1-\varrho_{\mathrm{eff}}^2}\right),\qquad(24)$$

and an analogous dependence for $\mathcal{L}_\perp$ is described by expression (5).

Now, let us consider the issue of SPR excitation in the cylinder and the spherocylinder. It is known [10] that the corresponding condition consists in the vanishing of the real part of the denominator in expression (3) for the polarizability tensor components, i.e.,

$$\mathrm{Re}\epsilon_{\perp(\parallel)} = -\frac{1-\mathcal{L}_{\perp(\parallel)}}{\mathcal{L}_{\perp(\parallel)}}\epsilon_{\mathrm{m}}.\qquad(25)$$

Whence it follows that both the longitudinal and transverse plasmon resonances can be excited in the analyzed nanoparticles.

In the non-dissipative approximation ($\gamma_{\mathrm{eff}}^{\perp(\parallel)}=0$), the formulas for the frequencies of the transverse and longitudinal SPRs look like

$$\omega_{sp}^{\perp(\parallel)} = \frac{\omega_p}{\sqrt{\epsilon^\infty+\frac{1-\mathcal{L}_{\perp(\parallel)}}{\mathcal{L}_{\perp(\parallel)}}\epsilon_{\mathrm{m}}}}.\qquad(26)$$

Below, formula (26) is used to compare the experimental results obtained for the frequencies of the transverse and longitudinal SPRs in a finite-length cylinder with the theoretical ones calculated in the framework of the model of equivalent prolate spheroid.

3. Calculation Results and Their Discussion

The frequency dependences of the polarizability and the absorption and scattering cross-sections for rod-like particles were calculated for Au, Ag, Cu and Al prolate spheroids, cylinders, and spherocylinders located in the Teflon matrix ($\epsilon_{\mathrm{m}}=2.3$). The parameters of the metals are given in Table 2.

Figures 2 and 3 illustrate the frequency dependences of the real and imaginary parts and the absolute values of the longitudinal and transverse, respectively, components of the polarizability tensor of Au nanoparticles in the form of prolate spheroids. Note that the real parts $\mathrm{Re}\,\alpha_{\perp(\parallel)}(\omega)$ change their sign in
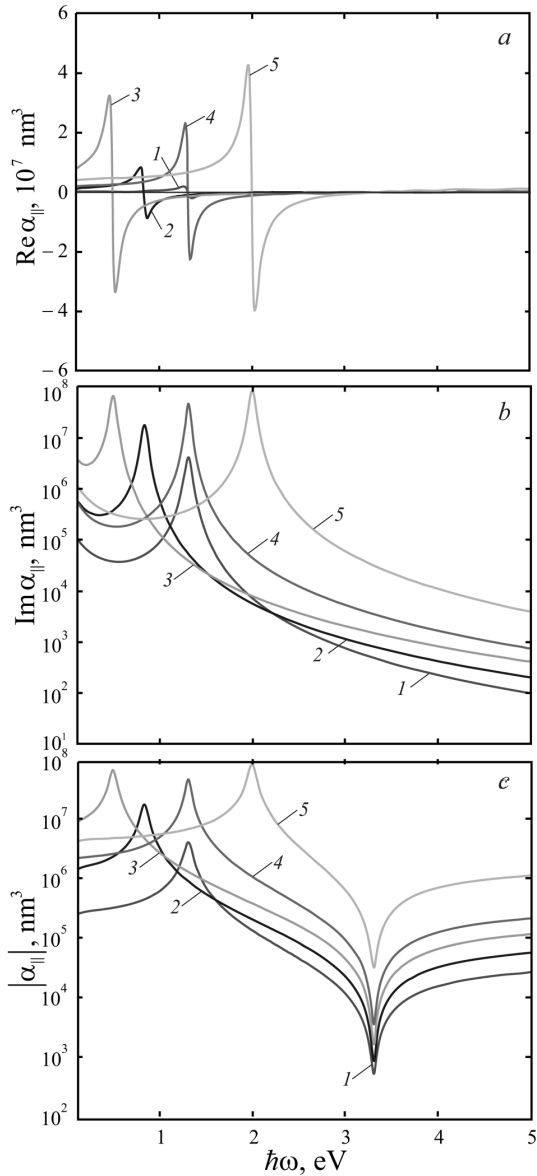
Fig. 2. Frequency dependences of the real (*a*) and imaginary (*b*) parts and the absolute value (*c*) of the longitudinal component of the polarizability of rod-like gold particles in the form of prolate spheroid: $b = 10$ nm, $a = 50$ nm (*1*); $b = 10$ nm, $a = 100$ nm (*2*); $b = 10$ nm, $a = 200$ nm (*3*); $b = 20$ nm, $a = 100$ nm (*4*); $b = 50$ nm, $a = 100$ nm (*5*)

Fig. 3. The same as in Fig. 2 but for the transverse component of the polarizability of rod-like gold particles in the form of prolate spheroid

the examined frequency interval (Figs. 2, *a* and 3, *a*), whereas the imaginary parts $\text{Im}\,\alpha_{\perp(\parallel)}(\omega) > 0$ there (Figs. 2, *b* and 3, *b*). Furthermore, the maxima of the imaginary parts of the longitudinal and transverse components of the polarizability tensor corre-
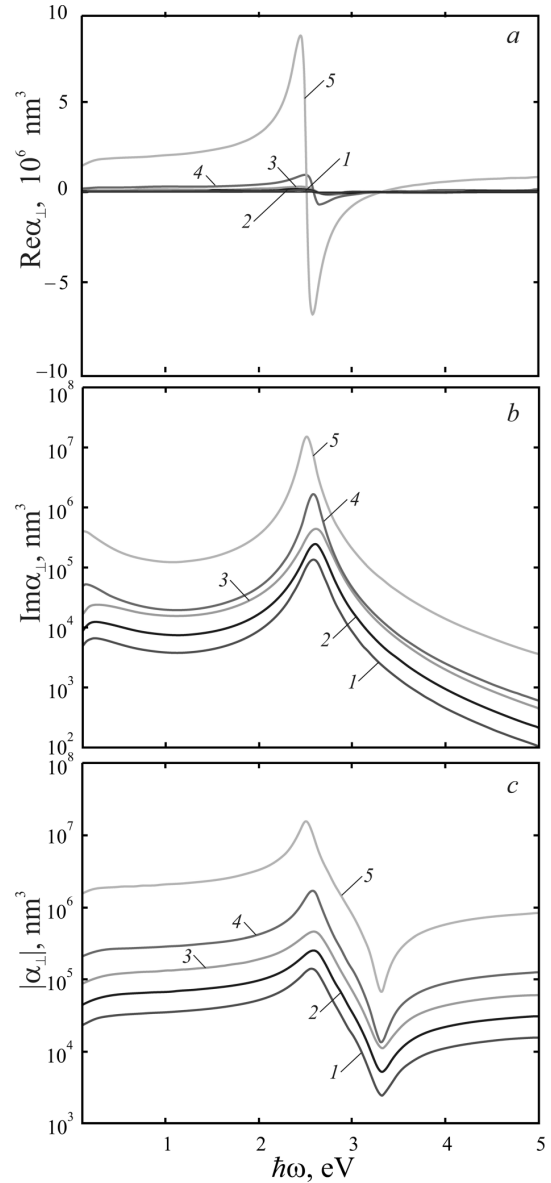
spond to the longitudinal and transverse SPRs. The calculation results testify that the position of the longitudinal SPR strongly depends on the lengths of the spheroid semi-axes, in contrast to the transverse SPR whose position practically does not change when the lengths of the semi-axes change, with $\omega_{sp}^{\perp} > \omega_{sp}^{\parallel}$ at that. In particular, if the aspect ratio increases, the sequences of curves $1 \rightarrow 2 \rightarrow 3$ and $5 \rightarrow 4 \rightarrow 2$
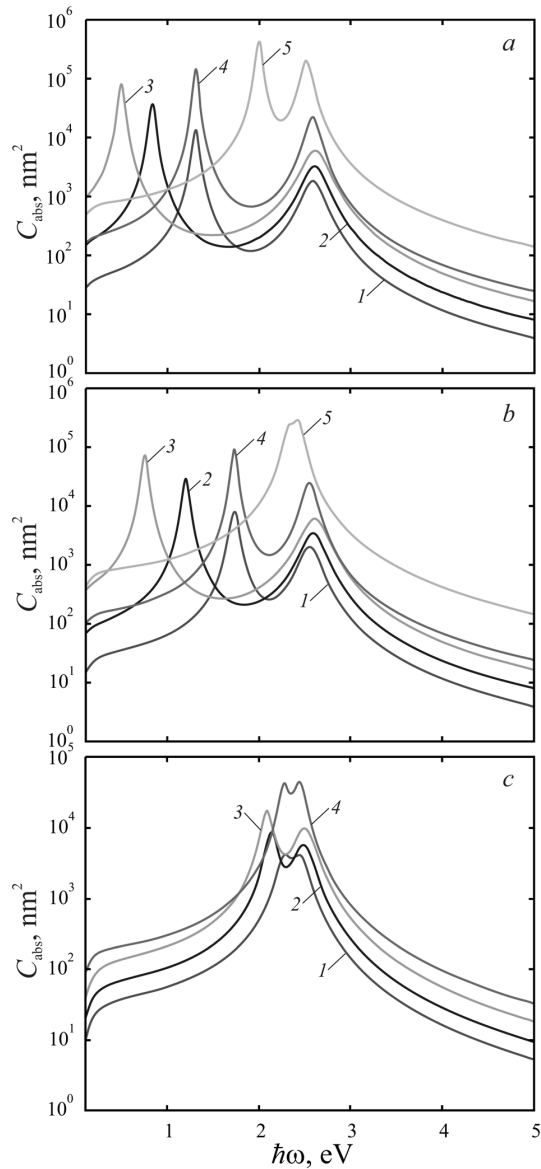
Fig. 4. Frequency dependences of the absorption cross-sections for prolate spheroids (*a*), cylinders (*b*), and spherocylinders (*c*). The parameters are the same as in Fig. 2

Fig. 5. The same as in Fig. 4 but for the scattering cross-sections

in Fig. 2, *b* demonstrate a "red" shift in the position of the longitudinal SPR. Hence we obtain that for a nanoparticle of this shape, the position of the longitudinal SPR, unlike the position of the transverse SPR, can be varied by changing the aspect ratio.

The curves describing the frequency dependences of the absolute values of the longitudinal and transverse components of the polarizability tensor (Figs. 2, *c* and
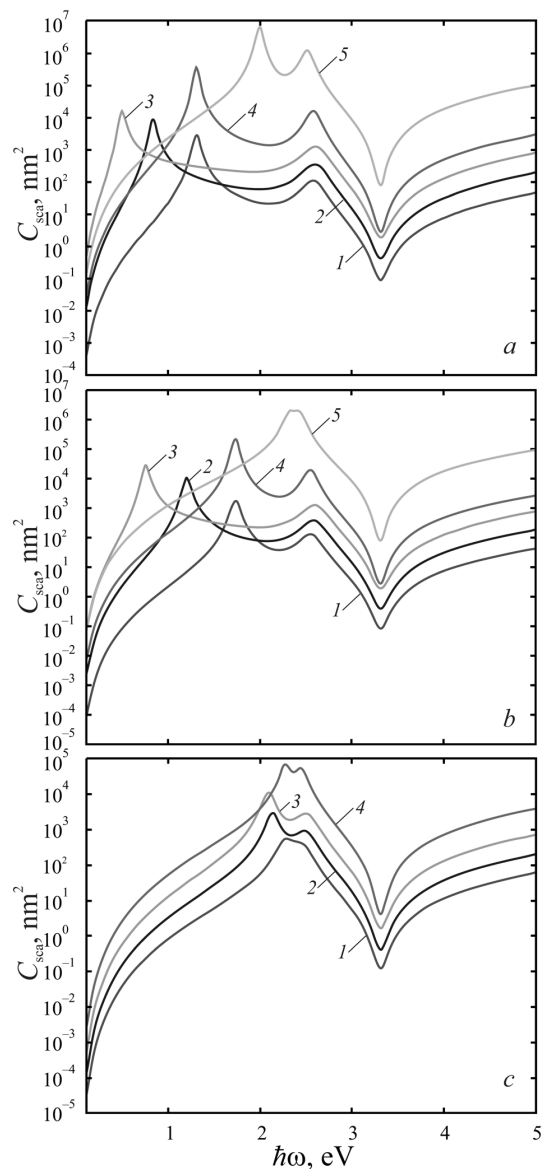
3, *c*) are similar to the curves for $\mathrm{Re}\,\alpha_{\perp(\parallel)}(\omega)$ (they also have a maximum and a minimum), as well as to the curves for $\mathrm{Im}\,\alpha_{\perp(\parallel)}(\omega)$ (the positions of the maxima and the shifts (or their absence) of the maxima when the aspect ratio changes).

Analogous dependences for the absorption and scattering cross-sections of prolate spheroids, cylinders, and spherocylinders with various sizes are shown in Figs. 4 and 5, respectively. Since, according to for-

mula (1), $C_{abs} = \mathrm{Im}\left(\frac{2}{3}\alpha_\perp + \frac{1}{3}\alpha_\parallel\right)$, the curves $C_{abs}(\omega)$ have two maxima corresponding to the longitudinal and transverse SPRs (Fig. 4), with the "blue" shift of the first maxima in the absorption cross-section occurring when the aspect ratio of the spheroid increases (Fig. 4, *a*). The same effect takes place for finite-length cylinders (Fig. 4, *b*) and spherocylinders (Fig. 4, *c*) when the aspect ratio of the equivalent prolate spheroid increases. The only difference consists in that two close maxima merge into a single one for cylinders with $l = 2r$, whereas this case has no sense for spherocylinders because the spherocylinder degenerates into a sphere at $l = 2r$.

It should also be noted that the distances between the first and second maxima in the absorption cross-sections decrease along the sequence "prolate spheroid $\rightarrow$ cylinder $\rightarrow$ spherocylinder" (Fig. 4). As for the position of the second maximum, it is practically independent of the lengths of the minor and major semi-axes in both a spheroidal particle and a prolate spheroid equivalent to the cylinder and the spherocylinder. Those facts testify that the first maximum in the absorption cross-section corresponds to the longitudinal SPR, and the second one to the transverse SPR.

The curves $C_{sca}(\omega)$ depicted in Fig. 5 are qualitatively similar to the curves $|\alpha_\perp(\omega)|$ and $|\alpha_\parallel(\omega)|$, and the positions of the first and second maxima and their shifts with the variation of the aspect ratio correspond to analogous curves $C_{abs}(\omega)$ for nanoparticles of all examined shapes. Note that similarly to the frequency dependences of the absorption cross-sections, the dependences of the scattering cross-sections have the same features for prolate spheroids (Fig. 5, *a*), cylinders (Fig. 5, *b*), and spherocylinders (Fig. 5, *c*).

The frequency dependences of the absorption cross-section for the particles of various geometries, cylindrical particles of various metals, and cylindrical Al particles with various effective electron masses are shown in Fig. 6. The first maximum in the dependence $C_{abs}(\omega)$ is characterized by a "blue" shift along the particle shape sequence "prolate spheroid $\rightarrow$ $\rightarrow$ cylinder $\rightarrow$ spherocylinder"; at the same time, the "red" shift of the second maximum is insignificant in this case. As a result, the distance between the maxima in the absorption cross-section substantially decreases along the indicated sequence (Fig. 6, *a*). The blue shift of the first maxima in the absorption cross-section along the series of metals
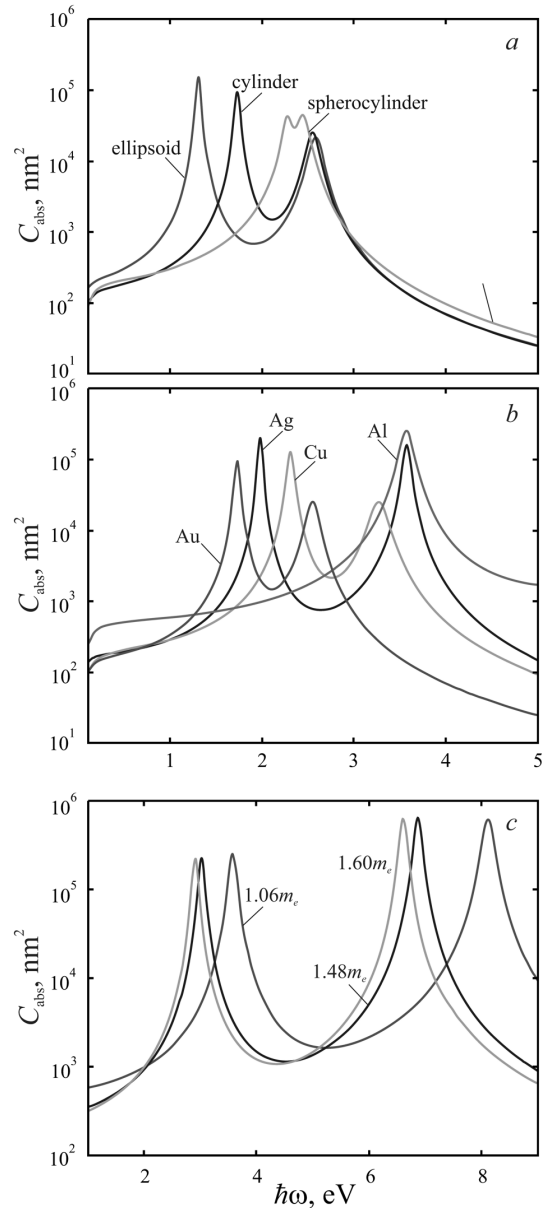

Fig. 6. Frequency dependences of the absorption cross-sections for particles of various shapes with $b = 20$ nm and $a = 100$ nm (*a*), cylinders with $b_r = 20$ nm and $a_l = 100$ nm made of various metals (*b*), and Al cylinders with $b_r = 20$ nm, $a_l = 100$ nm, and various values of the effective electron mass (*c*)

Au $\rightarrow$ Ag $\rightarrow$ Cu $\rightarrow$ Al is a consequence of the relationships $\omega_p^{Au} < \omega_p^{Ag} < \omega_p^{Cu} < \omega_p^{Al}$ (Fig. 6, *b*). In cylindrical Al particles (Fig. 6, *c*), as the effective electron mass increases, the first and second max-

Table 3. **Longitudinal and transverse SPR frequencies for rod-like nanoparticles at various aspect ratio values**

ϱ	Prolate spheroid	
	$\omega_{sp}^{\parallel}$, eV	$\omega_{sp}^{\perp}$, eV
0.05	0.486	2.6
0.10	0.825	2.593
0.15	1.089	2.585
0.20	1.299	2.575
0.25	1.471	2.564
0.30	1.612	2.553
0.35	1.730	2.541
0.40	1.830	2.530
0.45	1.916	2.518
0.50	1.989	2.506

ϱ	Cylinder	
	$\omega_{sp}^{\parallel}$, eV	$\omega_{sp}^{\perp}$, eV
0.05	0.433	2.601
0.10	0.743	2.595
0.15	0.990	2.588
0.20	1.192	2.580
0.25	1.360	2.571
0.30	1.501	2.562
0.35	1.620	2.552
0.40	1.723	2.542
0.45	1.811	2.532
0.50	1.888	2.522

ϱ	Spherocylinder	
	$\omega_{sp}^{\parallel}$, eV	$\omega_{sp}^{\perp}$, eV
0.05	2.062	2.492
0.10	2.078	2.488
0.15	2.095	2.485
0.20	2.112	2.481
0.25	2.129	2.477
0.30	2.146	2.473
0.35	2.163	2.468
0.40	2.180	2.464
0.45	2.196	2.459
0.50	2.213	2.454

Fig. 7. Calculated dependences of the longitudinal SPR frequency on the inverse aspect ratio: the "prolate spheroid" model (the shape parameter is the aspect ratio ϱ) (*1*); the "equivalent prolate spheroid" model (the shape parameter is the effective aspect ratio ϱ_{eff}) (*2*); symbols correspond to experimental results taken from work [26]

cies $\omega_{sp}^{\perp(\parallel)}$) owing to the increase of the effective electron mass.

The results of calculations for the frequencies of the longitudinal and transverse SPRs for the particles of the considered shapes are given in Table 3. As one can see, with the growth of the aspect ratio, the frequencies of the longitudinal and transverse SPRs get closer and the distance between the resonances decreases along the shape sequence "cylinder → prolate spheroid → spherocylinder".

Figure 7 illustrates a comparison of experimental data with the results of theoretical calculations obtained for the shape dependence of the longitudinal SPR frequency in the cases of a cylinder considered in the framework of the "prolate spheroid" model (curve *1*) and the "equivalent prolate spheroid" model (curve *2*). The results demonstrate the proximity of experimental points to curve *2*, which confirms the adequacy of the "equivalent prolate spheroid" model to the real situation and the validity of this approach.

4. Conclusions

Analytical expressions for the frequency dependences of the transverse and longitudinal components of the polarizability tensor and the absorption and scatter-

ima in the absorption cross-section undergo a "red" shift associated with a reduction in the frequency of bulk plasmons (and, accordingly, the SPR frequen-
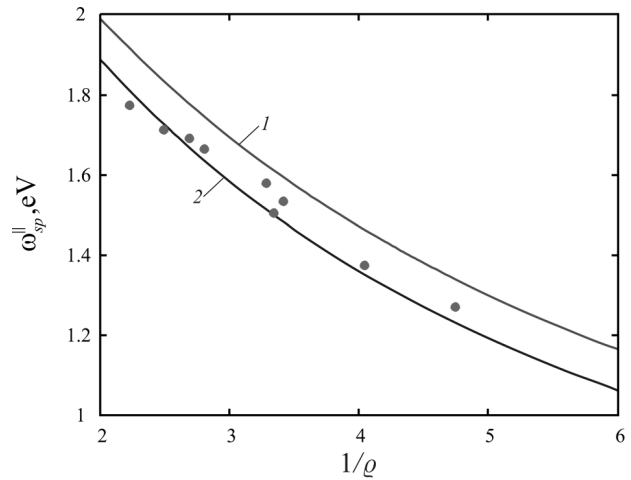
ing cross-sections of finite-length cylinders and spherocylinders have been obtained in the framework of the model of equivalent prolate spheroid. It is shown that the position of the longitudinal SPR substantially depends on the lengths of the spheroid semi-axes, whereas the position of the transverse SPR practically does not change at that. Therefore, the position of the longitudinal SPR in rod-like structures can be adjusted by changing their aspect ratio.

It is found that the first maximum of the absorption cross-section corresponds to the longitudinal SPR, and the second one to the transverse SPR in nanoparticles of all considered shapes. Furthermore, the distance between the maxima in the absorption cross-section substantially decreases along the nanoparticle shape sequence from the prolate spheroid to the spherocylinder. It is demonstrated that the character of the SPR shift ("blue" or "red") depends on both the particle shape and the material the particle was made of.

It is shown that the application of the "equivalent prolate spheroid" model for the determination of the frequency of the longitudinal SPR makes it possible to achieve better agreement with the experiment without applying complicated computational approaches, e.g., the discrete dipole method, which was used in work [26].

1. L. Novotny, B. Hecht. *Principles of Nano-Optics, 2nd ed.* (Cambridge University Press, 2012).

2. J.W. Haus. Introduction to nanophotonics. In: *Fundamentals and Applications of Nanophotonics* (Woodhead Publishing, 2016).

3. J. Yan, X. Liu, C. Ma, Y. Huang, G. Yang. All-dielectric materials and related nanophotonic applications. *Mater. Sci. Eng. R Rep.* **141**, 100563 (2020).

4. M. Sun, H. Dong, A.W. Dougherty, Q. Lu, D. Peng, W.T. Wong, B. Huang, L.D. Sun, C.H. Yan. Nanophotonic energy storage in upconversion nanoparticles. *Nano Energy* **56**, 473 (2019).

5. J. Xavier, S. Vincent, F. Meder, F. Vollmer. Advances in optoplasmonic sensors – combining optical nano/microcavities and photonic crystals with plasmonic nanostructures and nanoparticles. *Nanophotonics* **7**, 1 (2018).

6. H. Zhao, L.K. Chin, Y. Shi, P.Y. Liu, Y. Zhang, H. Cai, E.P.H. Yap, W. Ser, A.Q. Liu. Continuous optical sorting of nanoscale biomolecules in integrated microfluidic-nanophotonic chips. *Sens. Actuat. B Chem.* **331**, 129428 (2021).

7. F. Pisanello. Implantable micro and nanophotonic devices: toward a new generation of neural interfaces. *Microelectron. Eng.* **215**, 110979 (2019).

8. E. Luan, H. Shoman, D.M. Ratner, K.C. Cheung, L. Chrostowski. Silicon photonic biosensors using label-free detection. *Sensors* **18**, 3519 (2018).

9. U. Kreibig, M. Vollmer. *Optical Properties of Metal Clusters* (Springer, 1995).

10. S. Maier. *Plasmonics: Fundamentals and Applications* (Springer, 2007).

11. K.C. Grabar, R.G. Freeman, M.B. Hommer, M.J. Natan. Preparation and characterization of Au colloid monolayers. *Anal. Chem.* **67**, 735 (1995).

12. J.C. Hulteen, R.P. Van Duyne. Nanosphere lithography: A materials general fabrication process for periodic particle array surfaces. *J. Vac. Sci. Technol. A* **13**, 1553 (1995).

13. V. Bastys, I. Pastoriza-Santos, B. Rodriguez-Gonzalez, R. Vaisnoras, L.M. Liz-Marzan. Formation of silver nanoprisms with surface plasmons at communication wavelengths. *Adv. Funct. Mater.* **16**, 766 (2006).

14. B. Nikoobakht, M.A. El-Sayed. Preparation and growth mechanism of gold nanorods (NRs) using seed-mediated growth method. *Chem. Mater.* **15**, 1957 (2003).

15. Y.G. Sun, Y.N. Xia. Shape-controlled synthesis of gold and silver nanoparticles. *Science* **298**, 2176 (2002).

16. A.O. Koval, A.V. Korotun, Yu.A. Kunytskyi, V.A. Tatarenko, I.M. Titov. *Electrodynamics of Plasmon Effects in Nanomaterials* (Naukova Dumka, 2021) (in Ukrainian).

17. K.L. Kelly, E. Coronado, L.L. Zhao, G.C. Schatz. The optical properties of metal nanoparticles: the influence of size, shape, and dielectric environment. *J. Phys. Chem. B* **107**, 668 (2003).

18. N.K. Grady, N.J. Halas, P. Nordlander. Influence of dielectric function properties on the optical response of plasmon resonant metallic nanoparticles. *Chem. Phys. Lett.* **399**, 167 (2004).

19. N.I. Grigorchuk. Plasmon resonant light scattering on spheroidal metallic nanoparticle embedded in a dielectric matrix. *Europhys. Lett.* **97**, 45001 (2012).

20. P.M. Tomchuk. Dependence of light scattering cross-section by metal nanoparticles on their shape. *Ukr. J. Phys.* **57**, 553 (2012).

21. A.V. Korotun, A.A. Koval', I.N. Titov. Optical absorption of a composite based on bilayer metal-dielectric spherical nanoparticles. *J. Appl. Spectrosc.* **87**, 240 (2020).

22. A.V. Korotun, N.I. Pavlyshche. Cross sections for absorption and scattering of electromagnetic radiation by ensembles of metal nanoparticles of different shapes. *Phys. Met. Metallogr.* **122**, 941 (2021).

23. C.F. Landes, S. Link, M.B. Mohamed, B. Nikoobakht, M.A. El-Sayed. Some properties of spherical and rod-shaped semiconductor and metal nanocrystals. *Pure Appl. Chem.* **74**, 1675 (2002).

24. A.V. Korotun, Ya.V. Karandas, V.I. Reva, I.M. Titov. Polarizability of two-layer metal-oxide nanowires. *Ukr. J. Phys.* **66**, 906 (2021).

25. J.M. McLellan, Zh.-Y. Li, A.R. Siekkinen, Y. Xia. The SERS activity of a supported Ag nanocube strongly depends on its orientation relative to laser polarization. *Nano Lett.* **7**, 1013 (2007).

26. A.X. Wang, X. Kong. Review of recent progress of plasmonic materials and nano-structures for surface-enhanced raman scattering. *Materials* **8**, 3024 (2015).

27. E.S. Kolosovas-Machuca, A. Cuadrado, H.J. Ojeda-Galvan, L.C. Ortiz-Dosal, A.C. Hernandez-Arteaga, M.d.C. Rodriguez-Aranda, H.R. Navarro-Contreras, J. Alda, F.J. Gonzalez. Detection of histamine dihydrochloride at low concentrations using Raman spectroscopy enhanced by gold nanostars colloids. *Nanomaterials* **9**, 211 (2019).

28. A. Brioude, X.C. Jiang, M.P. Pileni. Optical properties of gold nanorods: DDA simulations supported by experiments. *J. Phys. Chem. B* **109**, 13138 (2005).

29. H. Chen, L. Shao, Q. Li, J. Wang. Gold nanorods and their plasmonic properties. *Chem. Soc. Rev.* **42**, 2679 (2013).

30. S.W. Prescott, P. Mulvaney. Gold nanorod extinction spectra. *J. Appl. Phys.* **99**, 123504 (2006).

31. C.L. Nehl, J.H. Hafner. Shape-dependent plasmon resonances of gold nanoparticles. *J. Mater. Chem.* **18**, 2415 (2008).

32. V. Myroshnychenko, J. Rodriguez-Fernandez, I. Pastoriza-Santos, A.M. Funston, C. Novo, P. Mulvaney, L.M. Liz-Marzan, F.J. Garcia de Abajo. Modelling the optical response of gold nanoparticles. *Chem. Soc. Rev.* **37**, 1792 (2008).

33. D. Constantin. Why the aspect ratio? Shape equivalence for the extinction spectra of gold nanoparticles. *Eur. Phys. J. E* **38**, 116 (2015).

34. N.I. Grigorchuk, P.M. Tomchuk. Optical and transport properties of spheroidal metal nanoparticles with account for the surface effect. *Phys. Rev. B* **84**, 085448 (2011).

35. N.I. Grigorchuk. Radiative damping of surface plasmon resonance in spheroidal metallic nanoparticle embedded in a dielectric medium. *J. Opt. Soc. Am. B* **29**, 3404 (2012).

А.В. Коротун, Я.В. Карандась, В.І. Рева

АНАЛІТИЧНА ТЕОРІЯ ПЛАЗМОННИХ ЕФЕКТІВ У СТРИЖНЕПОДІБНИХ МЕТАЛЕВИХ НАНОЧАСТИНКАХ. МОДЕЛЬ ЕКВІВАЛЕНТНОГО СФЕРОЇДА

В рамках моделі еквівалентного витягнутого сфероїда отримано аналітичні вирази для поляризовностей стрижнеподібних металевих структур, що дозволило суттєво спростити розрахунки їх оптичних характеристик. Розраховано частотні залежності поперечної та поздовжньої компоненти тензора поляризовності, а також перерізів поглинання і розсіювання для витягнутих сфероїдів, циліндрів та сфероциліндрів. Проаналізовано зміну положень максимумів уявної частини компонентів тензора поляризовності, перерізів поглинання та розсіювання при зміні розмірів, форми і матеріалу наночастинок. Встановлено, що положення поперечного поверхневого плазмонного резонансу в стрижнеподібних наночастинках форм, що розглядаються, практично нечутливе до зміни величин півосей, у той час як збільшення аспектного відношення приводить до "червоного" зсуву поздовжнього поверхневого плазмонного резонансу. Показано, що використання моделі еквівалентного витягнутого сфероїда дає задовільне узгодження між результатами розрахунків та експериментальними даними для частот поздовжнього поверхневого плазмонного резонансу, не потребуючи застосування складних обчислювальних методів.

К л ю ч о в і с л о в а: тензор поляризовності, перерізи поглинання та розсіювання, еквівалентний витягнутий сфероїд, швидкість релаксації, плазмонний резонанс.